Tuning the mechanical properties of dicyanamide-based molecular perovskites

Article

Accepted Version

Tuning the Mechanical Properties of Dicyanamide-Based Molecular Perovskites

Shivani Grover,[‡a] Stefan Burger,[‡b] Keith T. Butler,[c] Karina Hemmer,[b] Pia Vervoorts,[b] Gregor Kieslich*[b] and Ricardo Grau-Crespo*[a]

[a] *Department of Chemistry, Food and Pharmacy, University of Reading, United Kingdom, RG66DX, UK.*

[b] *Department of Chemistry, Technical University of Munich, Lichtenbergstraße 4, 85748 Garching, GER.*

[c] *Materials Research Institute, School of Engineering and Materials Science, Queen Mary University of London, Mile End Road, London E1 4NS, UK.*

[‡] Shared contribution

Corresponding Authors

*r.grau-crespo@reading.ac.uk
*gregor.kieslich@tum.de

ABSTRACT

ABX_3 molecular perovskites have recently gained attention in the field of ferroelectrics and barocalorics where the materials' mechanical properties such as mechanical stability, compressibility, hardness, and elasticity are important performance criteria. Akin to previous work on ceramic perovskites, research on molecular perovskites benefits from the modular building principle of the perovskite motif, enabling systematic studies to learn about the interplay of chemical composition, structure, and properties. Here we use the molecular perovskite series $[(n\text{Pr})_3(CH_3)N]M(C_2N_3)_3$ (nPr = –(C_3H_7) and M^{2+}= Mn, Co, Fe, Ni, Zn, Cd, Ba, Sr, Ca, Hg, or Mg) as a model system to study the impact of the M^{2+} metal species on the mechanical properties via lattice dynamic calculations and high-pressure powder X-ray diffraction. By using the bulk modulus as a proxy, we observe a relationship between geometric factors and mechanical properties that agree with chemical intuition. The results present a step forward for gradually refining our understanding of these materials, and contribute to the long-term goal, the design of material with targeted macroscopic properties.

INTRODUCTION

ABX$_3$ molecular perovskites, where *A* and/or *X* are molecular moieties, have attracted increased attention in recent years.[1] Research on molecular perovskites such as $[(NH_2)_2CH]Mn(HCOO)_3$,[2] $[N(CH_3)_4][Cd(N_3)_3]$,[3] and $[(NH_2)_3C]Mn(H_2POO)_3$,[4] has drawn inspiration from decades of research in the oxide perovskites, but with the additional benefit of the chemical space as offered by the inclusion of molecular units in the crystal structure,[5] as illustrated in Figure 1. Conceptually, the use of molecular *A*- and *X*-site species enhances the structural and chemical diversity in these perovskites, leading to new opportunities for tuning macroscopic material behaviour.[6] Examples are tilt-and-shift engineering to impart ferroelectric properties,[7, 8] tunability of hydrogen bonding interactions[9] between the A-site cation and the 3D $[BX_3]^-$ network with ramifications on the mechanical response,[10, 11] adjustable phase transition thermodynamics,[12, 13] and varying structural complexities[14] amongst others.

The mechanical properties of molecular perovskites have been demonstrated to be tuneable through different components of the material.[15] For instance, the larger elastic moduli and hardness of $[C(NH_2)_3]Mn(HCOO)_3$ compared to $[(CH_2)_3NH_2]Mn(HCOO)_3$ have been attributed to the larger number of hydrogen bonding interactions,[16] and a similar conclusion can be drawn for the elastic moduli across the A-site solid solution series $[NH_3NH_2]_{1-x}[NH_3OH]Zn(HCOO)_3$.[17] Looking at the impact of the metal ion, a linear correlation between the elastic moduli and ligand field stabilisation energy has been observed for the series $[(CH_3)_2NH_2]M(HCOO)_3$ with M^{2+} = Mn^{2+}, Co^{2+}, Ni^{2+} and Zn^{2+}.[18] Likewise, the bulk modulus of several molecular perovskites series, such as $[(CH_3)_2NH_2][M(HCOO)_3$ (M^{2+} = Mn^{2+}, Fe^{2+} and Cu^{2+}) [19], $[(C_3H_7)_4N]M(C_2N_3)_3$ (M^{2+} = Mn^{2+} and Cd^{2+}),[20, 21] $[(NH_2)_3C]M(HCOO)_3$ (M^{2+} = Mn^{2+}, Co^{2+} and Cd^{2+})[22, 23] have been explored by high-pressure diffraction experiments on single crystals and powders. Some studies[24, 25] have reported trends such as a relationship between size and chemistry of the divalent B-site metal and the bulk modulus, which agree with chemical intuition. Furthermore, the impact of B-site metal defects has been studied by comparing $[C(NH_2)_3]Mn(HCOO)_3$ with its defective analogue $[C(NH_2)_3]Fe_{2/3}\square_{1/3}(HCOO)_3$, (□ = vacancy), which exhibits a bulk modulus that is nearly 30% lower.[26] This body of work demonstrates the immense potential for tailoring the mechanical properties in hybrid and molecular perovskites, depending on a solid understanding of the chemical and physical principles that affect them.

More recently, molecular perovskites such as $[(C_3H_7)_4N]Mn(C_2N_3)_3$ and $[(C_3H_7)_4N]Cd(C_2N_3)_3$ have emerged as model systems in barocalorics, where their modular building principle enables to search for crystal chemistry factors that determine a material's performance in solid-state cooling.[27, 28] A relation between compressibility and barocaloric performance has recently been implied,[29] an intuitive link when considering the barocaloric coefficient dT_c/dp as a proxy. A softer material is thus expected to exhibit a larger barocaloric coefficient, a rule which provides a useful guideline to manipulate barocaloric performance in the future. Therefore, the identification of

crystal chemistry principles that determine a molecular perovskite's mechanical response, *i.e.* its structural response to pressure such as compressibility or similarly the bulk modulus, is an important step forward in the search for intuitive material design guidelines.

In the present work, we study the mechanical properties of the molecular perovskite series $[(n\mathrm{Pr})_3(CH_3)N]M(C_2N_3)_3$, (*n*Pr = –($C_3H_7$) and M^{2+}= Mn, Co, Fe, Ni, Zn, Cd, Ba, Sr, Ca, Hg, or Mg), combining density functional theory (DFT) simulations with high pressure powder X-ray diffraction (HPPXRD). Previously we have shown that $[(n\mathrm{Pr})_3(CH_3)N]M(C_2N_3)_3$ can crystallise in two polymorphs, and in this work we focus on the thermodynamically stable rhombohedral compound, which exhibits an order-disorder phase transition related to $[(n\mathrm{Pr})_3(CH_3)N]^+$. Via HPPXRD we determine the experimental bulk moduli for M^{2+}= Mn, Co and Ni and apply DFT simulations to obtain the bulk modulus for an extended range of compositions. We find a strong trend relating the mechanical properties to the B-site Shannon radius and the B-X bond length, with higher-order perturbations to this dominant trend from ligand-field stabilisation energy. Our results agree with chemical intuition and with recently published barocaloric performances of related compounds such as $[(C_3H_7)_4N]Mn(C_2N_3)_3$ and $[(C_3H_7)_4N]Cd(C_2N_3)_3$.

Results and discussion

We start by elucidating the experimental and computational bulk moduli of the molecular perovskite series $[(n\mathrm{Pr})_3(CH_3)N]M(C_2N_3)_3$ (M^{2+} = Mn^{2+}, Co^{2+} Ni^{2+}). The materials $[(n\mathrm{Pr})_3(CH_3)N]M(C_2N_3)_3$ (M^{2+} = Mn^{2+}, Co^{2+} and Ni^{2+}) were synthesised according to the strategy established in our recent work.[30] In its low temperature modification, the thermodynamic stable polymorph of $[(n\mathrm{Pr})_3(CH_3)N]M(C_2N_3)_3$ crystallises in the space-group *R*3c. The divalent metal M^{2+} is in an octahedral coordination from six nitrogen atoms forming a 3D ReO_3-type $[M(C_2N_3)_3]^-$ network, see Figure 1a. The A-site cation $[(n\mathrm{Pr})_3(CH_3)N]^+$ sits in the void of the ReO_3-network, forming the perovskite structure motif. At T_c= 284 K (Mn^{2+}), 301 K (Co^{2+}) and 312 K (Ni^{2+}), $[(n\mathrm{Pr})_3(CH_3)N]M(C_2N_3)_3$ exhibits a temperature-driven order-disorder phase transition related to the A-site cation to the centrosymmetric space-group $R\bar{3}c$. HPPXRD experiments were performed by using the "pressure jump cell",[31] which enables the collection of HPPXRD data between ambient pressure and 0.4 GPa with a fine pressure resolution, see Figure 1b for a representative contour plot and supporting information for further details. Lattice parameter and volume *V* as

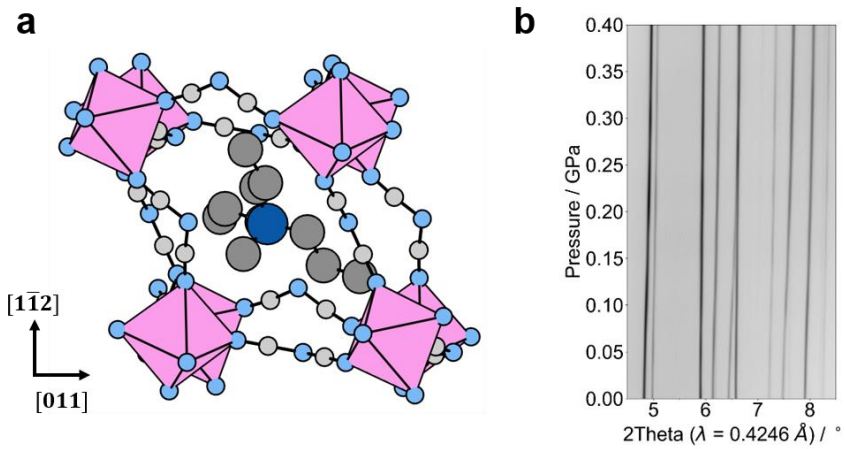

Figure 1. (**a**) Crystal structure of $[N(C_3H_7)_3CH_3]Mn(C_2N_3)_3$ illustrating the 3D pseudo-cubic ReO_3-type $[M(C_2N_3)_3]^-$ network. In (**b**), HPPXRD pattern in the pressure range p = ambient – 0.4 GPa of $[N(C_3H_7)_3CH_3]Mn(C_2N_3)_3$ are shown as a contour plot and HPPXRD data of all materials including lattice parameters from Pawley profile fits are given in the supporting information. Colour scheme: C atoms of $C_2N_3^-$ in light grey, C atoms of $[N(C_3H_7)_3CH_3]^+$ in dark grey, N atoms of $C_2N_3^-$ in light blue, N atom of $[N(C_3H_7)_3CH_3]^+$ in dark blue, MnN_6 octahedra pink, and H atoms are omitted for clarity.

a function of pressure were extracted by Pawley profile fits to HPPXRD data, see Table 1 and supporting information (SI). Given that HPPXRD experiments were performed at approximately 300 K, a pressure-driven phase transition from the high-temperature to the low-temperature polymorph can be expected for $[(n\text{Pr})_3(CH_3)N]Mn(C_2N_3)_3$ and $[(n\text{Pr})_3(CH_3)N]Co(C_2N_3)_3$ at low pressures;[30] however, due to the similarities between X-ray powder diffraction pattern of both phases, we used Ff-plots to identify the onset of the phase transition, see SI. The bulk moduli of the high-pressure (low-temperature) phases were determined by fitting $V(p)$ data to the Birch-Murnaghan equation of state (2nd order), and the results are shown in Table 2. We observe a decreasing unit cell volume and an increasing bulk modulus when going along the series Mn^{2+}, Co^{2+} and Ni^{2+}. This trend agrees with chemical intuition: a higher packing density coming from a reduced metal radius leads to a higher bulk modulus, *i.e.* a lower compressibility.

Table 1. Comparison of experimental and computationally obtained lattice parameters. Experimental values are taken from single crystal X-ray diffraction experiments at 100 K [30] whereas the calculations ignore vibrational effects and therefore are formally at 0 K (and without any zero-point contributions).

	$M = Mn^{2+}$			$M = Co^{2+}$			$M = Ni^{2+}$		
Parameter	Exp.	Theory	Error	Exp.	Theory	Error	Exp.	Theory	Error
a / Å	10.36	10.28	-0.77%	10.26	10.19	-0.68%	10.22	10.16	-0.58%
α / deg	76.47	77.24	-1.0%	76.28	77.13	-1.11%	76.01	76.76	0.98%
V / Å^3	1033.54	1017.39	-1.56%	1001.57	988.71	-1.28%	986.49	976.46	-1.02%

Table 2. Bulk modulus (B) for $[N(C_3H_7)_3CH_3]M(C_2N_3)_3$ as determined from theory and experiment. For $M = Mn^{2+}$ and Co^{2+}, the bulk moduli were extracted from the high-pressure phase, i.e. the pressure regime p = 0.125 – 0.4 GPa (Mn^{2+}) and 0.1 – 0.4 GPa (Co^{2+}), see supporting information for more details.

B / GPa	$M = Mn^{2+}$	$M = Co^{2+}$	$M = Ni^{2+}$
Theory	11.0±0.1	12.5±0.1	13.4±0.1
Experiment	7.08 ± 0.15	9.90 ± 0.30	10.85 ± 0.16

In order to obtain bulk moduli via density functional theory (DFT), we used the low-temperature experimental structures as starting point for geometry optimisation; see supporting information. The obtained lattice parameters are in good agreement with the experimental values, with the inclusion of the Hubbard *U* correction improving the outcomes to errors below 2%. The bulk moduli were obtained by fitting DFT energy (*E*) vs. volume (*V*). For each point the

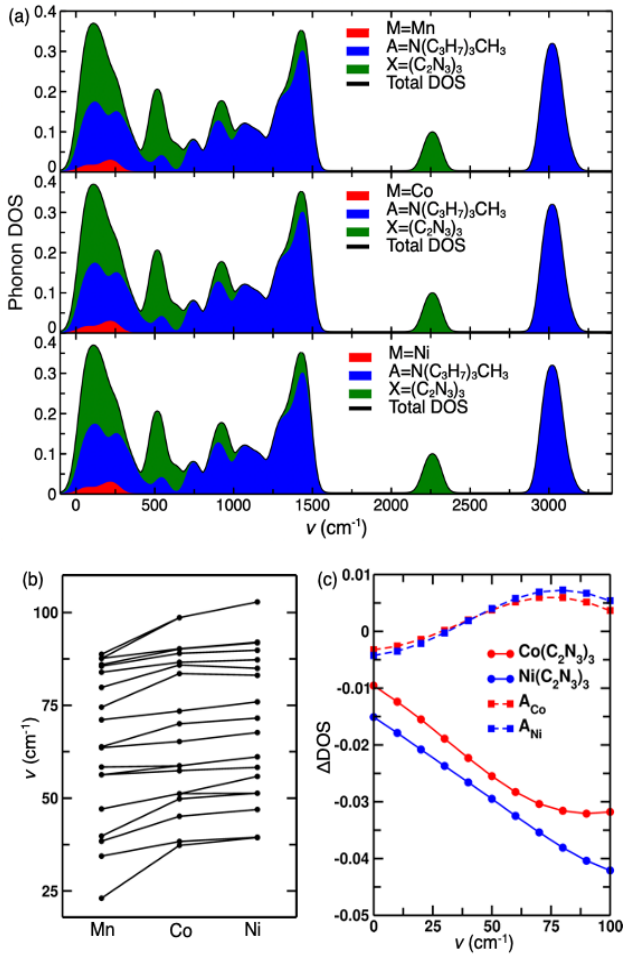

Figure 2. Vibrational properties of $[N(C_3H_7)_3CH_3]M(C_2N_3)_3$ perovskites (M = Mn, Co and Ni). (**a**) Phonon density of states, (**b**) zone-centre vibrational frequency of the soft modes for the three compositions, (**c**) ΔDOS of the $Co(C_2N_3)_3$ and $Ni(C_2N_3)_3$ framework with $Mn(C_2N_3)_3$ framework as reference and ΔDOS from the A-site of Co and Ni substituted system with respect to Mn containing system.

structure was relaxed by optimising cell parameters and atomic coordinates at a fixed volume. The fitting of $E(V)$ data for $[(n\text{Pr})_3(CH_3)N]Mn(C_2N_3)_3$, $[(n\text{Pr})_3(CH_3)N]Co(C_2N_3)_3$ and $[(n\text{Pr})_3(CH_3)N]Ni(C_2N_3)_3$ is shown in Figure S1 in the SI. The bulk moduli obtained at each composition are listed in Table 2 and compared to experimental outcomes, showing that results from DFT calculations reproduce the trend of experimentally determined bulk moduli. The overestimation of absolute values of bulk modulus can be, at least partially, ascribed to the underestimation of lattice parameters within the level of theory employed, since more tightly packed structures show larger moduli. Table 1 shows that our DFT (GGA+U) calculations indeed predict slightly underestimated cell parameters (although note that experimental lattice parameters have been taken from structures at 100 K, while lattice parameters from DFT are formally at 0 K, ignore also any zero-point vibrational effects).

The analysis above suggests a close relationship between crystal packing and mechanical properties. To further explore this effect and provide mechanistic insights, we have performed lattice dynamics calculations to obtain phonon spectra. The phonon density of states (pDoS) for the three compositions is shown in Figure 2a. The pDoS has been decomposed into contributions from A-site cation, B-site metal cation and X-site linker anion by using Phonopy[32]. All three materials have qualitatively a similar pDoS, with the metal centre contribution only observed at low frequencies (up to 300 cm^{-1}) which is related to higher atomic mass of the *M* compared to the other species in the material. From the zone-centre vibrational frequencies, a clear hardening of the soft optical modes $\upsilon < 100\ \mathrm{cm}^{-1}$ is observed from Mn to Co and Ni, as shown in Figure 2b. To better understand the origin of these differences, the contributions to the pDoS of the 3D $[M(C_2N_3)_3]^-$ framework and A-site cation is calculated, see Figure 2c. It is evident that the soft modes are dominated by the 3D framework only, where $[(n\text{Pr})_3(CH_3)N]Mn(C_2N_3)_3$ has the greatest pDoS at low frequencies, followed by $[(n\text{Pr})_3(CH_3)N]Co(C_2N_3)_3$ and then $[(n\text{Pr})_3(CH_3)N]Ni(C_2N_3)_3$. This trend in the low-frequency pDoS matches well with the trend in bulk modulus and supports the assertion that altering the framework by metal cation substitution provides a precise handle for tuning mechanical properties. This finding agrees with previous work on the effects of B-X bonding on the mechanical properties of hybrid and molecular perovskites. It has been shown that stiffer B-X bonds achieved through greater ligand-field stabilisation[18, 33] or through greater electronegativity differences properties[11, 34, 35] result in stiffer materials. The direct effect of B-X bonding on the bulk modulus suggests that it would be interesting to investigate how crystal chemistry can be used to alter the mechanical properties across a range of different chemical environments.

Having established the importance of the nature of the metal cation in determining the mechanical and vibrational properties in these molecular perovskite systems, the next question is whether this trend extends to other metal species and if examining a wider range of compositions can allow us to draw stronger inferences about the origin of the effect. Therefore, we have explored a range of hypothetical $[(n\text{Pr})_3(CH_3)N]M(C_2N_3)_3$ materials, where the

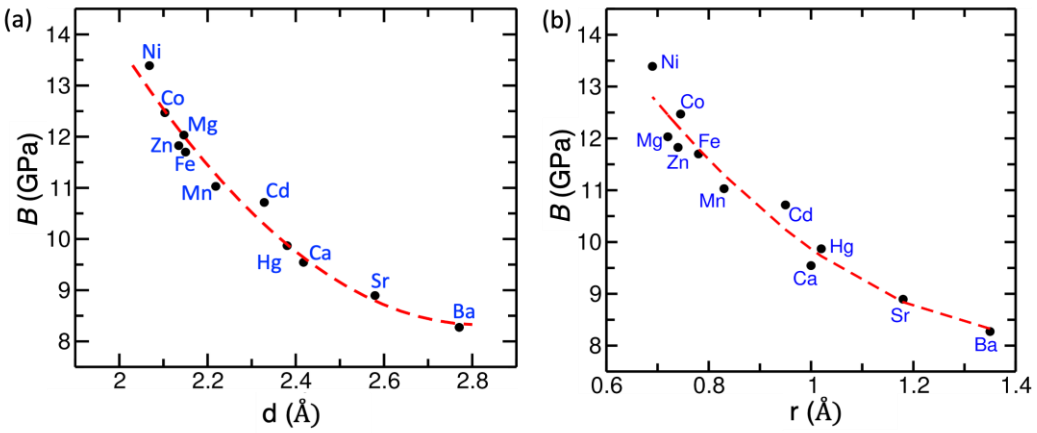

Figure 3. Bulk modulus, *B*, as a function of (**a**) equilibrium metal-linker bond distance, *d*, and (**b**) Shannon radius, *r*, of M cations for $[N(C_3H_7)_3CH_3]M(C_2N_3)_3$ perovskites.

mechanical properties can be modified by cation substitution at the *M* site. We extend our computational simulations to systems containing other metals: Fe^{2+}, Zn^{2+}, Cd^{2+}, Ba^{2+}, Sr^{2+}, Ca^{2+}, Hg^{2+}, or Mg^{2+}, and determine their bulk modulus using DFT calculations. These hypothetical structures are not necessarily stable experimentally, due to size and electron configuration effects. However, we can examine them computationally as we can constrain the symmetry of the system so that the metal forms an octahedral complex with $C_2N_3^-$ linker anion to form the desired phase, as we are interested here in establishing the trend rather than in predicting real materials.

In Figure 3 the variation in bulk modulus for various metal systems is shown. The Ba-containing system has the lowest bulk modulus (8.3 GPa), with the Ni- containing system having the highest value of 13.4 GP among the systems of interest considered here. To examine the geometric factors determining the mechanical behaviour in this molecular perovskite series, we plot the variation in bulk modulus as a function of *M*-N bond length in MN_6 octahedra (metal-linker bond distance), *d*. This shows that the larger the *M*-N bond distance, the smaller the bulk modulus (see Figure 3a). This finding is similar to the situation in hybrid lead halide perovskites, where the stiffness, as measured by the Young modulus, decreases with the lead-to-halide bond length.[34] We further look at the variation in bulk modulus as a function of Shannon radius (*r*) of the *M* cation, see Figure 3b. Clearly, the Shannon radius is a good predictor of the bulk modulus in this series of compounds. The small differences between the relationships shown in Figure 3 a and b partially arise from deviations in the additivity rule of ionic radii due to covalency effects (e.g. Co and Zn have similar ionic radii, but Co-N bonds can be expected to be slightly more covalent than Zn-N bonds because of the smaller electronegativity difference). The observation of the correlation of the bulk modulus with the Shannon radius is useful because Shannon radii are available a priori, without the need for a DFT optimization.

CONCLUSION

We have calculated the mechanical and vibrational properties of a molecular perovskite series, which are of importance for the potential application of these materials for barocaloric applications. We establish that the bulk modulus depends on the phonon density of states of the $[MX_3]^-$ framework and specifically the metal-linker bond. Our analysis shows that the material with the softest phonon modes corresponds to the material with the lowest bulk modulus. Given the importance of the metal cation determining the vibrational and mechanical properties we extend our study to a series of hypothetical materials with other metals in oxidation state II: Fe, Zn, Cd, Ba, Sr, Ca, Hg, and Mg. These calculations reveal a clear relationship between the metal-linker bond length and the bulk modulus. Furthermore, we show that the Shannon radius of a metal, which can be known *a priori*, without calculations or experiments, is a good descriptor for how the bulk modulus will depend on composition.

The obtained dependence of the bulk modulus on the metal-to-nitrogen bond distance agrees with chemical intuition and provides a starting point for rational materials design of molecular perovskites with tailored mechanical properties. Other factors such as the preferred crystal structure, presence of defects, microstructure and vibrational properties will also contribute to the overall mechanical properties of the systems. However, to a first order it should be possible to carefully change the mechanical properties by metal substitution. We also emphasise that the metal does not need to be substituted completely; solid solutions are a powerful approach to continuously tailoring materials properties, and we expect that solid solutions could be a promising materials design strategy in these systems.

Methods

Computational Details. Our calculations are based on density functional theory (DFT) as implemented in the Vienna Ab Initio Simulation Package (VASP).[36,37] The exchange-correlation energy of electrons is treated within the generalized gradient approximation (GGA) with the functional by Perdew, Burke, and Ernzerhof (PBE).[38] In order to account for the limitations of the GGA to describe the d orbitals of transition metals, we included Hubbard corrections for these orbitals (GGA+U), following the formalism introduced by Dudarev et al.,[39] where a single parameter (U_{eff}) controls the strength of the correction. The U_{eff} parameters for Mn (4.0 eV), Co (3.3 eV), Fe (4 eV) and Ni (6.4 eV) were taken from the work by Wang et al.,[40] where they were fitted so that GGA+U could reproduce the experimental oxidation energies in transition metal oxides. We also included the dispersion corrections following Grimme's D3 scheme.[41] The

projector augmented wave (PAW) method[42, 43] was used to describe the interactions between the valence electrons and the frozen cores, which consisted of orbitals up to 2p for C and N, and up to 3d for the transition metals. We used an energy cutoff of 520 eV to truncate the planewave expansion of the Kohn-Sham wavefunctions, which is 30% above the default cutoff for the employed PAW potentials, to minimize Pulay errors. Brillouin Zone (BZ) integrations were performed by sampling the reciprocal space using a $\Gamma-$ centred mesh of $4 \times 4 \times 4$ k-points with reference to rhombohedral unit cell. Spin polarization was allowed in all calculations.

Experimental Methods. Samples were synthesised by applying a solution-based slow crystallisation method with details about precursors, concentrations, etc. in the supporting information. Pressure-dependent powder X-ray diffraction patterns in the range from ambient pressure to 0.4 GPa were collected using the pressure jump-cell,[30] a dedicated setup for exploring high pressure properties of soft materials.[44] Cell parameters for each pressure point were extracted by a Pawley profile fit analysis as implemented in TOPAS v6[30] and *V*(*p*) data was fitted to a second-order Birch-Murnaghan equation of state by using the EoSFit7c software.[45]

AUTHOR INFORMATION

R.G.-C., K.T.B. and G.K. designed the study. S.G. carried out the DFT calculations. S.B. synthesised the samples and performed sample analysis. K.H. and P.V. assisted with synchrotron data collection. All authors contributed to the interpretation of experimental and computational results and to the writing of the manuscript.

ACKNOWLEDGMENTS

S.G. is grateful for a doctoral studentship from the Felix Trust. This work made use of ARCHER, the UK's national high-performance computing service, *via* the UK's HPC Materials Chemistry Consortium, which is funded by EPSRC (EP/R029431), and of the Young supercomputer, *via* the UK's Materials and Molecular Modelling Hub, which is partially funded by EPSRC (EP/T022213/1). S.B. is grateful for holding a doctoral scholarship from the Hanns-Seidel Foundation. K.H. thanks the 'Fonds der Chemischen Industrie' for a PhD fellowship. G.K. would also like to thank the 'Fonds der Chemischen Industrie' for support through the Liebig Fellowship scheme.

REFERENCES

1. W. Li, Z. Wang, F. Deschler, S. Gao, R. H. Friend and A. K. Cheetham, *Nat. Rev. Mater.*, 2017, **2**, 16099.

2. M. Mączka, A. Ciupa, A. Gągor, A. Sieradzki, A. Pikul, B. Macalik and M. Drozd, *Inorg. Chem.*, 2014, **53**, 5260-5268.
3. Z.-Y. Du, Y.-P. Zhao, W.-X. Zhang, H.-L. Zhou, C.-T. He, W. Xue, B.-Y. Wang and X.-M. Chen, *Chem. Comm.*, 2014, **50**, 1989-1991.
4. Y. Wu, S. Shaker, F. Brivio, R. Murugavel, P. D. Bristowe and A. K. Cheetham, *J. Am. Chem. Soc.*, 2017, **139**, 16999-17002.
5. G. Kieslich and A. L. Goodwin, *Mater. Horiz.*, 2017, **4**, 362-366.
6. S. Burger, K. Hemmer, D. C. Mayer, P. Vervoorts, D. Daisenberger, J. K. Zaręba and G. Kieslich, *Adv. Funct. Mater.*, 2022, **n/a**, 2205343.
7. H. L. B. Boström, M. S. Senn and A. L. Goodwin, *Nat. Commun.*, 2018, **9**, 2380.
8. H. L. B. Boström, *CrystEngComm*, 2020, **22**, 961-968.
9. K. L. Svane, A. C. Forse, C. P. Grey, G. Kieslich, A. K. Cheetham, A. Walsh and K. T. Butler, *J. Phys. Chem. Lett.*, 2017, **8**, 6154-6159.
10. L.-J. Ji, S.-J. Sun, Y. Qin, K. Li and W. Li, *Coord. Chem. Rev.*, 2019, **391**, 15-29.
11. J. Feng, *APL Mater.*, 2014, **2**, 081801.
12. K. T. Butler, K. Svane, G. Kieslich, A. K. Cheetham and A. Walsh, *Phys. Rev. B*, 2016, **94**, 180103.
13. G. Kieslich, J. M. Skelton, J. Armstrong, Y. Wu, F. Wei, K. L. Svane, A. Walsh and K. T. Butler, *Chem. Mater.*, 2018, **30**, 8782-8788.
14. S. A. Hallweger, C. Kaußler and G. Kieslich, *Phys. Chem. Chem. Phys.*, 2022, **24**, 9196-9202.
15. W. Li, S. Henke and A. K. Cheetham, *APL Mater.*, 2014, **2**, 123902.
16. W. Li, A. Thirumurugan, P. T. Barton, Z. Lin, S. Henke, H. H. M. Yeung, M. T. Wharmby, E. G. Bithell, C. J. Howard and A. K. Cheetham, *J. Am. Chem. Soc.*, 2014, **136**, 7801-7804.
17. G. Kieslich, S. Kumagai, A. C. Forse, S. Sun, S. Henke, M. Yamashita, C. P. Grey and A. K. Cheetham, *Chem. Sci.*, 2016, **7**, 5108-5112.
18. J.-C. Tan, P. Jain and A. K. Cheetham, *Dalton Trans.*, 2012, **41**, 3949-3952.
19. I. E. Collings, M. Bykov, E. Bykova, M. Hanfland, S. van Smaalen, L. Dubrovinsky and N. Dubrovinskaia, *CrystEngComm*, 2018, **20**, 3512-3521.
20. M. Mączka, I. E. Collings, F. F. Leite and W. Paraguassu, *Dalton Trans.*, 2019, **48**, 9072-9078.
21. M. Mączka, M. Ptak, A. Gągor, A. Sieradzki, P. Peksa, G. Usevicius, M. Simenas, F. F. Leite and W. Paraguassu, *J. Mater. Chem. C*, 2019, **7**, 2408-2420.
22. H. Gao, C. Li, L. Li, W. Wei, Y. Tan and Y. Tang, *Dalton Trans.*, 2020, **49**, 7228-7233.
23. Z. Yang, G. Cai, C. L. Bull, M. G. Tucker, M. T. Dove, A. Friedrich and A. E. Phillips, *Philos. Trans. Royal Soc.*, 2019, **377**, 20180227.
24. M. Mączka, M. Kryś, S. Sobczak, D. L. M. Vasconcelos, P. T. C. Freire and A. Katrusiak, *J. Phys. Chem. C*, 2021, **125**, 26958-26966.
25. M. Mączka, S. Sobczak, M. Kryś, F. F. Leite, W. Paraguassu and A. Katrusiak, *J. Phys. Chem. C*, 2021, **125**, 10121-10129.
26. H. L. B. Boström and G. Kieslich, *J. Phys. Chem. C*, 2021, **125**, 1467-1471.
27. J. M. Bermúdez-García, M. Sánchez-Andújar and M. A. Señarís-Rodríguez, *J. Phys. Chem. Lett.*, 2017, **8**, 4419-4423.
28. J. M. Bermúdez-García, M. Sánchez-Andújar, S. Castro-García, J. López-Beceiro, R. Artiaga and M. A. Señarís-Rodríguez, *Nat. Commun.*, 2017, **8**.

29. B. Li, Y. Kawakita, S. Ohira-Kawamura, T. Sugahara, H. Wang, J. Wang, Y. Chen, S. I. Kawaguchi, S. Kawaguchi, K. Ohara, K. Li, D. Yu, R. Mole, T. Hattori, T. Kikuchi, S.-i. Yano, Z. Zhang, Z. Zhang, W. Ren, S. Lin, O. Sakata, K. Nakajima and Z. Zhang, *Nature*, 2019, **567**, 506-510.
30. S. Burger, S. Grover, K. T. Butler, H. L. B. Boström, R. Grau-Crespo and G. Kieslich, *Mater. Horiz.*, 2021, **8**, 2444-2450.
31. N. J. Brooks, B. L. L. E. Gauthe, N. J. Terrill, S. E. Rogers, R. H. Templer, O. Ces and J. M. Seddon, *Rev. Sci. Instrum.*, 2010, **81**, 064103.
32. A. Togo and I. Tanaka, *Scr. Mater.*, 2015, **108**, 1-5.
33. G. Feng, D. Gui and W. Li, *Cryst. Growth. Des.*, 2018, **18**, 4890-4895.
34. S. Sun, F. H. Isikgor, Z. Deng, F. Wei, G. Kieslich, P. D. Bristowe, J. Ouyang and A. K. Cheetham, *ChemSusChem*, 2017, **10**, 3740-3745.
35. S. Sun, Y. Fang, G. Kieslich, T. J. White and A. K. Cheetham, *J. Mater. Chem. A*, 2015, **3**, 18450-18455.
36. G. Kresse and J. Furthmüller, *Phys. Rev. B*, 1996, **54**, 11169-11186.
37. G. Kresse and J. Furthmüller, *Comput. Mater. Sci.*, 1996, **6**, 15-50.
38. J. P. Perdew, K. Burke and M. Ernzerhof, *Phys. Rev. Lett.*, 1996, **77**, 3865-3868.
39. S. L. Dudarev, G. A. Botton, S. Y. Savrasov, C. J. Humphreys and A. P. Sutton, *Phys. Rev. B*, 1998, **57**, 1505-1509.
40. L. Wang, T. Maxisch and G. Ceder, *Phys. Rev. B*, 2006, **73**, 195107.
41. S. Grimme, J. Antony, S. Ehrlich and H. Krieg, *J. Chem. Phys.*, 2010, **132**, 154104.
42. P. E. Blöchl, *Phys. Rev. B*, 1994, **50**, 17953-17979.
43. G. Kresse and D. Joubert, *Phys. Rev. B*, 1999, **59**, 1758-1775.
44. P. Vervoorts, J. Stebani, A. S. J. Méndez and G. Kieslich, *ACS Materials Lett.*, 2021, **3**, 1635-1651.
45. R. J. Angel, M. Alvaro and J. Gonzalez-Platas, *Z. Kristallogr. – Cryst. Mater.*, 2014, **229**, 405-419.